Cold diffuse interstellar medium of Magellanic Clouds: I. HD molecule and cosmic-ray ionization rate

D. N. Kosenko,[★] S. A. Balashev,[†]

Ioffe Institute, 26 Politeknicheskaya st., St. Petersburg, 194021, Russia

ABSTRACT

HD molecule is one the most abundant molecule in the Universe and due to its sensibility to the conditions in the medium, it can be used to constrain physical parameters in the medium where HD resides. Lately we have shown that HD abundance can be enhanced in the low metallicity medium. Large and Small Magellanic Clouds give us an opportunity to study low metallicity galaxies in details towards different sightlines due to their proximity to our Galaxy. We revisited FUSE space telescope archival spectra towards bright stars in Magellanic Clouds to search for HD molecules, associated with the medium of these galaxies. We reanalysed H_2 absorption lines and constrained HD column density at the positions of H_2 components. We detected HD towards 24 sightlines (including 19 new detections). We try to measure cosmic ray ionization rate for several systems using measured $N(HD)/N(H_2)$, and in most cases get loose constraints due to insufficient quality of the FUSE spectra.

Key words: galaxies: ISM; ISM: molecules; cosmic rays

1 INTRODUCTION

The physical state of interstellar medium (ISM) is in the close relationship with the galaxy evolution, since it determines the star-formation, a key process of galaxy formation. On the other hand, stars influence environment around, by enrichment of the ISM with metals and dust, supply of the ultraviolet (UV) radiation and cosmic rays, energy and momentum injection etc. These change rates of reactions in the ISM, and hence impact on the abundances and level populations of the species. Therefore spectroscopic analysis of latter gives us opportunity to constrain the physical conditions in the observed systems, using comparison with the models.

Star-formation occurs in the molecular gas, which predominantly consists of H_2, which is hard to observe in the emission in cold ISM. Hence usually other tracers of H_2 are used, out of which CO is most abundant ($n(CO)/n(H_2) \lesssim 10^{-4}$, where $n(X)$ – is a number density of species) and exhaustively studied. However, H_2 can be easily observed in absorption using UV resonant transition (see recent note by Shull 2022). Unlike CO, H_2 in UV band predominantly probes diffuse molecular and translucent medium, due to saturation effects and associated extinction. However, such gas is certainly in intimate connection with the dense molecular gas, either providing its supply, or being the remnants of the intermittent molecular clouds.

Similar to H_2, HD – an isotopologue of H_2 with abundance $n(HD)/n(H_2) \sim 10^{-5}$, can be detected in the absorption using resonant transitions in UV band in our Galaxy (e.g. Snow et al. 2008) and in optical band at high redshifts (e.g. Varshalovich et al. 2001; Tumlinson et al. 2010; Ivanchik et al. 2015; Noterdaeme et al. 2017; Kosenko et al. 2021, and references therein). The importance of HD for ISM studies has been discussed starting from its detection (e.g.

Black & Dalgarno 1973; Hartquist et al. 1978), since HD provides an opportunity to constrain physical conditions in the medium, associated with absorption systems. Indeed, at the moderate presence of H_2, HD molecules form through a fast ion-molecular reaction[1]:

$$H_2 + D^+ \longrightarrow HD + H^+, \tag{1}$$

and destructed by photodissociation. This makes relative abundance of HD/H_2 sensitive to the main physical conditions in the medium, namely, number density, n, UV field intensity, χ, abundance of metals (and their depletion), and cosmic ray ionisation rate (CRIR), ζ. Regarding the latter, cosmic rays determine H^+ formation, which defines the ionized deuterium, D^+ abundance through charge exchange reaction, and therefore CRIR directly affects HD production rate.

Using a balance equation between HD formation (adding formation on the dust grains, which may be sufficient on the edge of the cloud, where there H_2 abundance is small $n(H_2)/n_{tot} \lesssim 10^{-4}$, and rate of reaction 1 is negligible) and destruction by UV radiation (taking into account self-shielding) we have recently obtained a simple semi-analytical formalism for dependence of HD/H_2 abundance on the aforementioned parameters (Balashev & Kosenko 2020) which allows us to constrain the physical conditions in the medium. One of the most important results of this recent study is that measured HD/H_2 ratios allow us to get constraints on CRIR in diffuse molecular medium of high-redshift galaxies.[2] therefore we have applied our method to a sample of all known HD/H_2 absorption systems at high redshifts (Kosenko et al. 2021). More intriguing, we also showed

---

[1] unlike H_2, which forms in the cold ISM mainly on the surface of dust grains

[2] Before that CRIR have been exhaustively explored in different environments, from diffuse neutral medium to dense prestellar clouds, in our Galaxy (e.g. Padovani et al. 2009; Indriolo & McCall 2012), but was constrained only for several sightlines in other galaxies, mostly representing the dense molecular gas (e.g. Muller et al. 2016; Shaw et al. 2016; Indriolo et al. 2018).

★ E-mail: kosenkodn@yandex.ru
† E-mail: s.balashev@gmail.com

that HD abundance is really enhanced in the low-metallicity medium probed by high-z Damped Lyman alpha (DLA) systems in comparison with high metallicities (Balashev & Kosenko 2020; Kosenko et al. 2021), as a consequence of enhanced ionization fractions. This behaviour of HD at low metallicity can be tested on the local dwarf galaxies, out of which the Large and Small Magellanic Clouds (LMC and SMC, respectively), seem to be the most appropriate, since they provide individually resolved stars due to their proximity to the Milky Way. Additionally, studies of diffuse gas with HD/H_2 provide us with valuable constraints on the physical conditions, which are known to differ much from our Galaxy.

LMC and SMC are the closest dwarf galaxies to the Milky Way. Distance to LMC is about 50 kpc (Pietrzyński et al. 2019) and it is a spiral galaxy with bar and bright dominant north spiral arm and a weak south arm. Average metallicity in the LMC is about 0.5 relative to solar (Russell & Dopita 1992). Most of the star-formation activity occurs in the bar and in the dominant arm, e.g. one of the most studied star-forming complex, 30 Dor, is located in the northeast of the bar. Distance to the SMC is about 62 kpc (Graczyk et al. 2020) and it is an irregular galaxy and can be divided to a bar (most dense, turbulent and UV exposed region of the SMC) and more quiescent and less dense wing on the east side. Metallicity of the SMC is about 0.2 relative to solar (Russell & Dopita 1992) and it is comparable with the average metallicity in the high redshift DLAs. From the east of the wing of SMC to the west side of the LMC there has been discovered Magellanic Bridge, a stream of neutral hydrogen with several stars (Hindman et al. 1963), which, as believed, was created due to the interaction between LMC and SMC about 200 Myr ago. Abundances in the Magellanic Bridge differ significantly from the abundances in both LMC and SMC and may be lower even then in the SMC (e.g. Lehner et al. 2008; Dufton et al. 2008; Lee et al. 2005; Ramachandran et al. 2021).

Proximity of Magellanic Clouds to our Galaxy gives us a perfect opportunity to study low metallicity galaxies in detail and to observe systems along different lines of sight within one galaxy. As we mentioned above, H_2 and HD are available in local Universe only using UV space telescopes. Fortunately, Far Ultraviolet Spectroscopic Explorer (FUSE) have been successfully used to study cold diffuse medium with HD and H_2 in the Milky Way (Snow et al. 2008; Shull et al. 2021) and with H_2 in Magellanic Clouds (Welty et al. 2012).

The main purpose of the work is to search for HD molecules in Magellanic Clouds using archival data obtained by FUSE telescope, to constrain HD/H_2 relative abundances in this satellite galaxies. Using measured HD and H_2 column density we tried to constrain cosmic ray ionization rates in the analysed systems. To our knowledge there was no attempt made to estimate CRIR in the Magellanic Clouds using the abundance matching. However, some constraints of cosmic-ray flux in LMC and SMC were obtained using gamma-ray radiation, that found average cosmic-ray density in both LMC and SMC lower then in Solar neighborhood (see e.g. Ackermann et al. 2016; Lopez et al. 2018). Nevertheless, one should bear in mind, that only cosmic rays with energies > 280 MeV contribute into gamma-ray flux due to pion decay, while ISM is ionized mostly by low-energy cosmic rays $\lesssim$ 100 MeV. Also low-energy cosmic rays may be trapped in the region where they were accelerated and their flux (and therefore CRIR) depends on the distance to the star-forming regions and supernova remnants. This paper is accompanied by another one (Kosenko in prep.), which is focused on the constraints on the number density and UV flux in LMC and SMC using the population of the rotational levels of H_2 (measured and presented in this paper) and C I fine-structure levels.

The paper is organized as follows: in Section 2 we describe a sample of data which was used in the work, in Section 3 we provide a description of the method to analyse observations, including line profile fitting. The results of data analysis, including new HD detections, are presented in Section 4. In the Section 5 we the describe constraint on the cosmic ray ionization rate obtained from measured HD/H_2 ratio. Section 6 we discuss how high resolution observations may improve obtained constraints, before summarizing the obtained results in Section 7.

2 DATA

HD and H_2 absorption lines fall into UV part of electromagnetic spectrum ($\lambda_{H_2} \lesssim 110$ nm), therefore observations of these molecules are limited due to the atmospheric absorption. The progress of H_2 observations in the Milky Way and the local Universe was certainly attributed to availability of the space UV telescopes. The best resolution and quality observations were performed by Far Ultraviolet Spectroscopic Explorer (FUSE, Moos et al. (2000); Sahnow et al. (2000)), which covers 907-1187 Å and have nominal spectral resolution $R \sim 20000$.

Blair et al. (2009) collected all of the FUSE observations in Magellanic Clouds and reprocessed them with the final calibration pipeline (CalFUSE 3.2) to get uniform data (FUSE Magellanic Clouds Legacy Project[3]). Using these data Welty et al. (2012) have found H_2 in 80 sightlines in LMC and in 65 sightlines in SMC. We selected those systems where $\log N_{H_2} \gtrsim 18$, since the quality of FUSE spectra does not allow detection of $\log N_{HD} \lesssim 13$ (typically measured relative abundance $N(HD)/N(H_2) \lesssim 10^{-5}$). This cut the sample to 48 sightlines in the LMC and 46 sightlines in the SMC.

The fully reduced spectra of the systems towards bright stars in LMC are available in the FUSE Magellanic Clouds Legacy Project (Blair et al. 2009). Typical observation of a star consists of the several exposures, obtained in different FUSE channels. We used spectra from 1A LiF channel, as it covers most of HD and H_2 absorption lines and has relatively high sensitivity (Dixon et al. 2007). Unfortunately, most of FUSE spectra suffer from inappropriate calibration issues, so we made an attempt to improve the quality of calibration. First, we find a zero-order spectrum, which is obtained by coadding of exposures, using the constant velocity shifts, that was found from the procedure of cross-correlation (Simkin 1974; Tonry & Davis 1979). From the zero-order spectrum we obtained rough estimates on H_2 column densities, Doppler parameters and redshifts. Then, using H_2 synthetic spectrum, constructed from these estimates, as a template, we obtained a wavelength dependent shifts for each exposure. We took only narrow, unblended lines and cross-correlated them with the template. The wavelength dependency of the estimated shifts was interpolated with piece-wise linear function, that was finally applied to correct the exposures, during coadding.

3 ANALYSIS

We model line profiles with standard multicomponent Voigt profile fitting using Monte Carlo Markov Chain (MCMC) sampler to obtain posterior distribution function of the absorption system parameters: column densities (N, measured throughout the paper in cm^{-2}), Doppler parameters, (b) and redshifts (z). The continuum was independently constructed for each considered fit (H_2, HD, etc) by B-splain interpolation of the neighboring regions of absorption

---

[3] https://archive.stsci.edu/prepds/fuse_mc/

lines, clear from the evident absorptions. We note that in the case of the saturated H_2 lines, which show Lorentzian wings this is a bit ambiguous task, therefore we iteratively adjusted continuum in the case of outlying lines. To construct the synthetic spectrum we used HD and H_2 transition lines and molecular data, collected by Ubachs et al. (2019).

To estimate parameters and its uncertainties we used maximum aposteriori probability and 68.3% credible intervals, respectively. We judge between detection and non detection of HD based on the constrained column density posterior probability function. For the cases where it shows a solitary peak we reported a measurement, while if there is a significant amount of the posterior near the lower end of column density range (taken to be $\log N(\mathrm{HD}) = 13$) we suggest an upper limit. Upper limits on column densities (where necessary) were found using one-sided 3σ (99.7%) credible interval. We note that reported in our study uncertainties are statistical ones, derived in particular model assumptions. Systematic uncertainties, arisen from continuum placement, particular choice of fitting spectral pixels, and component decomposition in some cases may dominate the statistical ones, therefore the latter should be taken with caution, especially in some systems, where it is found relatively small (in comparison to other systems). From the other side, since we used MCMC sampler to constrain the posterior distribution, we were able to explore a multimodal structure of the likelihood function and hence in some cases our constraints on column density are quite wide, since both non-saturated and saturated solutions provide the similar quality of the fit.

Firstly we refitted H_2 absorption lines, that typically corresponds to several lower rotational levels ($J \lesssim 5$) of the lowest vibrational state. In comparison with previous studies, where either only curve of growth analyses was used, or profiles were fitted only for the lower, $J = 0, 1$ levels, we performed the full joint profile fitting of all available levels. We used the same redshifts for all H_2 rotational levels, but allowed Doppler parameters to vary independently (except upper levels in several systems where the values were found to be unreasonably large). Additionally, we used the penalty functions (for details see, e.g. Noterdaeme et al. 2019; Kosenko et al. 2021) to favour a regular smooth shape of H_2 excitation diagram and an effect of increase of Doppler parameters with an increase of J, as was noticed before (e.g. Balashev et al. 2009; Noterdaeme et al. 2007).

The nominal resolution of spectra, obtained by FUSE is $R = \lambda/\Delta\lambda = 20000$, but we noticed that it can be reduced by a procedure of exposure coadding, calibration and other systematic effects of observations. So we made R to be an additional independent parameter during the fitting procedure. In the most cases, we found R below 20000, in the range $\sim 11000 - 18000$.

Using obtained velocity decomposition from H_2 profiles, we constrained the column density of HD molecules at the position of H_2 components. To fit HD column density we used priors on Doppler parameters from H_2 $J = 0$ (except systems where we detected HD) and fixed redshifts. One should note that many HD lines are blended, mostly by H_2, but also by metals; moreover some blends are attributed to the stellar absorptions.

4 RESULTS

In the spectra of stars towards Magellanic Clouds there are typically two groups of the components: one from Milky Way disk and/or halo and another from LMC or SMC. In most of the cases each group can be resolved into few sub-components, that was fitted with profile fitting. In total, HD was detected towards 24 sightlines (among which

in 19 there were new detections), and we placed upper limits on HD column densities in all others. The total H_2 and HD column densities derived from line profiles are shown in Tables 1 and 2 for LMC and SMC, respectively. Details on analysis of each systems are shown in Appendix A (see Supplementary materials). We show an example of line profile fitting of HD lines for the system towards Sk 191 in the SMC in the Figure 1; in the Appendix A we show all of the new HD detections. We also show an example of non-detection of HD lines in the Figure 2 in the system towards AV 14 in the SMC. In Figure 3 we show measured HD and H_2 column densities in the components and compared it with known measurement obtained in Milky Way and at high-redshifts. We note that since the resolution and spectral quality is not enough we predominantly obtained conservative limits on HD at the level $\log N(\mathrm{HD}) \lesssim 15 - 16$, which we also show in Figure 3.

We found a wide (≈ 2 dex) range of measured HD/H_2 ratios in Magellanic Clouds from the values below the Milky-Way measurements, to the values higher that the isotopic D/H ratio. However, at the intermediate H_2 column densities, HD abundance is very sensitive to the physical conditions (see Balashev & Kosenko 2020), due to the sensitivity of the position of D/HD transition, and therefore is not a problem to explain such wide range. We additionally, note that there is an obvious selection effect in Fig. 3, that is we were limited with $\log N(\mathrm{HD}) \gtrsim 13.5$.

In Figure 4 we present comparison of the total H_2 column density obtained by Welty et al. (2012) with the our results, obtained using the sum over all components associated with LMC and SMC. One can see that $N(H_2)$ values that we obtained are systematically higher (~ 0.3 dex) then that obtained by Welty et al. (2012). It may arise, firstly, from differences in methods: for most of the systems Welty et al. (2012) fitted only $J = 0$ and 1 lines and for only about 40 systems in their sample they provided detailed fit assuming multiple components. This may lead to underestimation of their results. Secondly, the discrepancy may arise from difference and difficulties in the calibration of data and uncertainty in resolution of combined spectra after reduction. Thirdly, as was noted above, in our analysis we used MCMC method, which in some cases provide the results with relatively low Doppler parameters and therefore may overestimate column densities (in the Tables 1 and 2 such systems are denoted by item e) in the case of the low column densities $\log N \lesssim 19$, at which Lorentz wings are not yet evident. Such low ($b \gtrsim 1\,\mathrm{km\,s^{-1}}$) Doppler parameters are not surprising for cold clouds, and sometimes confirmed in high-resolution observations (e.g. Carswell et al. 2011). The Doppler parameters, under FUSE resolution (corresponding $b \approx 20\,\mathrm{km\,s^{-1}}$) mainly estimated from joint fit of lines with different oscillator strengths. However, since the FUSE spectrum has limited spectral range and number of available H_2 bands is typically limited to few. Therefore, high-resolution observations with larger wavelength range are needed to confirm a realm of such low Doppler parameter values. And the last, Welty et al. (2012) have not provided uncertainties on their column densities and we do not know real inconsistency between our results.

Below we provide some details regarding several interesting sightlines.

4.1 Sk-67 5

The star is located in diffuse H II region on the Western edge of LMC and the system have previously been studied by André et al. (2004), who used data, obtained by FUSE, HST/STIS and VLT/UVES. They found $\log N(H_2) = 19.44 \pm 0.05$ which is in agreement with our value $\log N(H_2) = 19.47 \pm 0.01$. Their value of HD column density
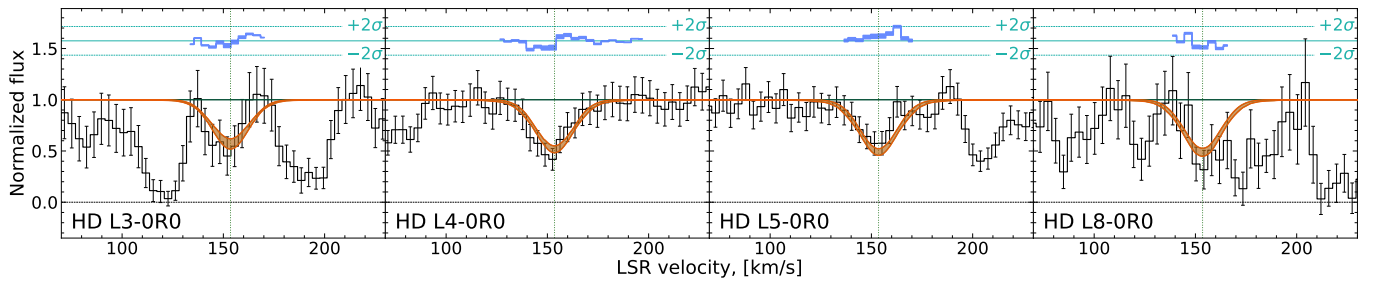
Figure 1. Fit to HD absorption lines towards Sk 191 in SMC. Here black line shows spectrum, while the coloured stripes show 0.683 credible interval of the line profiles sampled from posterior probability distributions of fitting parameters. The red represents the total line profile, while the green ones indicate individual components. In this particular spectrum, the green and red coincides, since there is only one component. Blue points at the top of each panel show residuals. Here we show only components found in Magellanic Clouds.
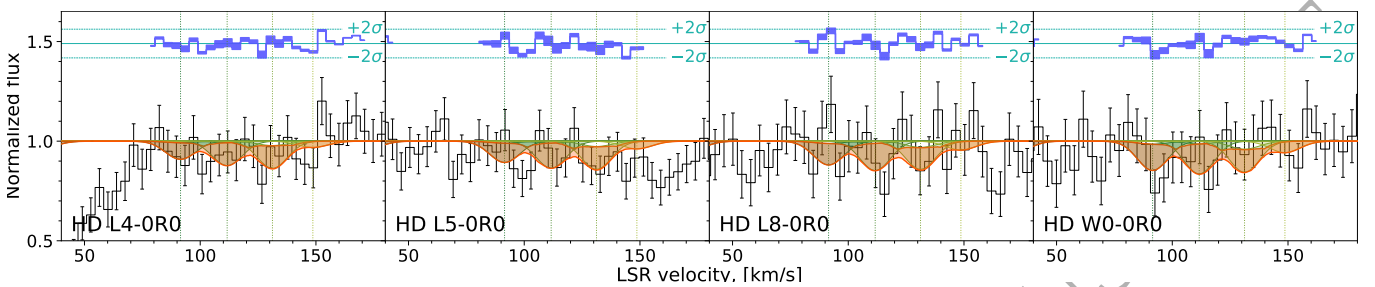
Figure 2. Fit to HD absorption lines towards AV 14 in SMC, which shows an example of non-detection of HD molecule. Lines are the same as for 1.

is $13.62^{+0.09}_{-0.12}$, while we obtained a wider range $15.5^{+0.3}_{-2.1}$, which includes saturated solution for the fit (see Sect. 3). Indeed, to obtain HD column density André et al. (2004) used an average value between Apparent Optical Depth (AOD, Savage & Sembach (1991)) method and line profile fitting, however it is known that AOD is not appropriate for lines with large optical depth and/or low resolution (above it was noted than resolution of FUSE spectra may be degraded after data reduction), therefore HD column density given by André et al. (2004) may be underestimated.

4.2 Sk-67 105

Sk-67 105 is one of the most massive eclipsing binary system (Niemela & Morrell 1986) in the LMC, which probably reveals a contact configuration with $48.3 M_\odot$ and $31.4 M_\odot$ (Ostrov & Lapasset 2003).

From H_2 lines (mostly from saturated J = 0 and 1) we found an evidence of partial coverage of absorption system towards Sk-67 105 which may arise from the configuration of the background radiation source. To get more reliable results we added a covering factor (see e.g. Balashev et al. 2011) as an independent parameter during the fit to H_2 lines, which value was found to be $0.888^{+0.002}_{-0.002}$. We could not detect HD in this system and placed upper limit on the column density in both H_2 components to be $\log N(\mathrm{HD}) \lesssim 14.8$ and $\lesssim 13.9$.

4.3 Sk-68 135

The star is located in the north of 30 Dor complex, one of the most studied star-forming regions and was previously studied by André et al. 2004.

Our HD column density estimate, $\log N(\mathrm{HD}) = 14.0^{+0.6}_{-0.3}$ is consistent with the result obtained by André et al. 2004, $\log N(\mathrm{HD}) = 14.15^{+0.11}_{-0.15}$, while we found H_2 column density to be a bit higher

(our $\log N(H_2) = 19.99 \pm 0.01$ versus their 19.87 ± 0.05; note that André et al. (2004) fitted H_2 assuming a single-component model, while we fitted H_2 with 2-components model). Roman-Duval et al. (2019) found $H\,\textsc{i}$ column density in this system to be significantly lower then Welty et al. (2012). Roman-Duval et al. (2019) used $Ly\alpha$ from HST, while Welty et al. (2012) used $Ly\beta$ line from FUSE spectra, where the difficulties in $H\,\textsc{i}$ column density estimation partly arises from large amount of H_2 absorption lines in the wings of $Ly\beta$. Additionally Welty et al. (2012) did not provide uncertainties of the $N(\mathrm{HI})$ measurements. Analysis of $Ly\alpha$ provides more reliable result, therefore we took value from Roman-Duval et al. (2019).

4.4 Sk-69 246

This star belongs to 30 Dor complex and the system on the line-of-sight have previously been studied by Bluhm & de Boer (2001) and André et al. (2004).

Bluhm & de Boer (2001) used curve-of-growth method to estimate H_2 and HD column densities. Nevertheless, we got $\log N(H_2) = 19.76 \pm 0.01$ and $\log N(\mathrm{HD}) = 13.89 \pm 0.06$ which is in agreement with results obtained by Bluhm & de Boer (2001). Comparing with André et al. (2004) we obtained that $\log N(H_2)$ is close to their result (19.66 ± 0.04). They found HD to be lower then both values found by Bluhm & de Boer (2001) and us. André et al. (2004) used only L5, L8 and L14 HD lines, while we used L3, L5, L7 and W0 (we did not use neither L14, since spectra from 1A LiF channel do not cover this line, moreover this line is weak and noizy nor L8 since it is blended by H_2 and S II absorptions). Also André et al. (2004) reported blend of L3 line, but we found that this line does not disagree with other HD lines so we included it in the analysis.
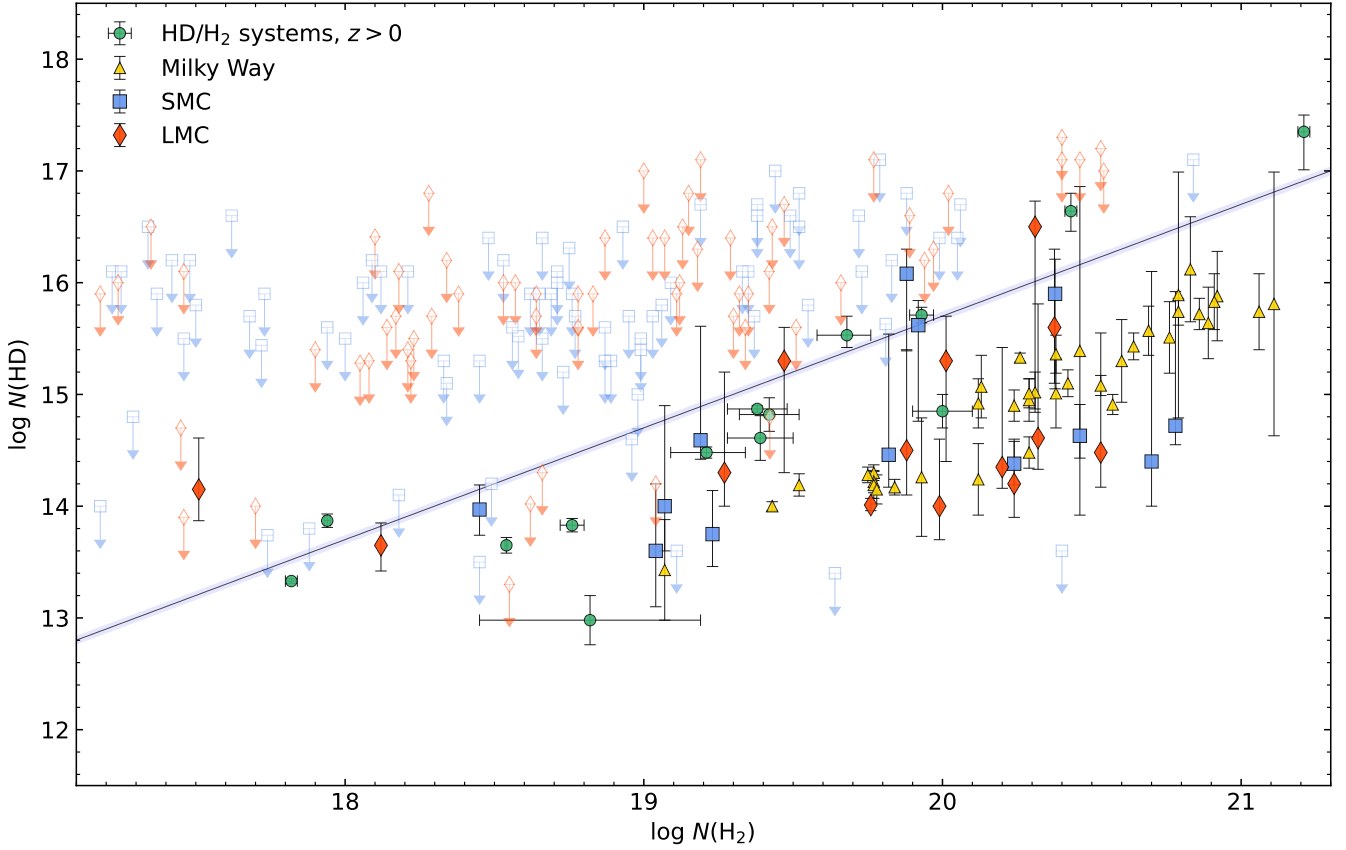
Figure 3. The HD versus H_2 column densities. The measurements in Small and Large Magellanic Clouds (this work) are shown by filled blue squares and red diamonds, respectively. Unfilled symbols represent the 3σ upper limits on HD column densities. Green circles show the measurements towards quasars at high redshifts (see Kosenko et al. 2021, and references therein), yellow triangles indicate the measurements in our Galaxy (Snow et al. 2008) and solid the blue line and stripe show the primordial D/H ratio (Planck Collaboration et al. 2020).

4.5 AV 95

The star AV 95 belongs to the bar of SMC and H_2 and HD in the system towards AV 95 have previously been studied by André et al. (2004).

Both our HD ($\log N(\mathrm{HD}) = 13.75^{+0.39}_{-0.29}$) and H_2 ($\log N(H_2) = 19.48^{+0.03}_{-0.02}$) column densities are consistent with values $\log N(H_2) = 19.43 \pm 0.04$ and $\log N(\mathrm{HD}) = 13.82^{+0.96}_{-0.18}$) found by André et al. (2004), respectively.

4.6 AV 242

The star AV 242 is located to the south-west of the star-formation region NGC 346 in the SMC and it is a bow shock-producing star, moving towards NGC 346 (Gvaramadze et al. 2011). Among the absorption systems towards AV 242 we found an evidence of the high (or intermediate) velocity cloud (HVC) at $v = 98.8$ km/s with $\log N(H_2) = 17.18^{+0.14}_{-0.16}$. To our knowledge, it is the first found HVC towards SMC, which contains H_2 molecules. Unfortunately, we could place only upper limits on the HD column density towards AV 242.

4.7 AV 488

The star AV 488 is located within Knot 1 region, in the wing of the SMC (a more quiescent region of SMC comparing with the bar).

Metals and H_2, HD and CO molecules have previously been studied by André et al. (2004). They have found H_2 and HD column densities to be 19.21 ± 0.06 and $13.85^{+0.11}_{-0.14}$, respectively, which consist with our results within errors (total H_2 column density is $19.30^{+0.01}_{-0.02}$ and HD $13.6^{+0.6}_{-0.5}$).

Table 1. Fit results for HD and H_2 towards LMC.

Star	$\log N\,(\mathrm{HI})^a$	ΔV^b, [km/s]	$\log N\,(\mathrm{H_2})$	$\log N\,(\mathrm{HD})^c$
Sk-67 2	21.00	260.5	$20.46^{+0.15}_{-0.46}$	$\lesssim 17.1$
'-'		280.3	$20.40^{+0.14}_{-0.20}$	$\lesssim 17.3$
Sk-67 5	21.00	294.7	$19.47^{+0.01}_{-0.01}$	$15.5^{+0.3}_{-2.1}$
Sk-66 1		286.3	$19.32^{+0.01}_{-0.01}$	$\lesssim 15.9$
Sk-67 20		283.2	$19.04^{+0.01}_{-0.01}$	$\lesssim 14.2$
Sk-66 18		274.5	$17.70^{+0.11}_{-0.12}$	$\lesssim 14.0$
		291.2	$18.17^{+0.05}_{-0.05}$	$\lesssim 15.7$
PGMW 3070		264.5	$18.14^{+0.04}_{-0.04}$	$\lesssim 15.6$
		286.5	$19.12^{+0.02}_{-0.01}$	$\lesssim 16.0$
LH 10-3073^{e,f}		265.5	$19.27^{+0.01}_{-0.03}$	$14.3^{+0.9}_{-0.3}$
		285.8	$18.05^{+0.17}_{-0.14}$	$\lesssim 15.3$
LH 10-3102^f		264.0	$17.51^{+0.11}_{-0.06}$	$14.2^{+0.4}_{-0.3}$
		285.0	$18.62^{+0.03}_{-0.01}$	$\lesssim 15.6$
		299.7	$14.65^{+0.07}_{-0.05}$	$\lesssim 15.7$
LH 10-3120	21.48^d	272.2	$18.22^{+0.03}_{-0.04}$	$\lesssim 15.3$
'-'		289.1	$17.90^{+0.07}_{-0.05}$	$\lesssim 15.4$
PGMW 3157		266.9	$17.35^{+0.25}_{-0.38}$	$\lesssim 16.5$
		287.2	$19.13^{+0.03}_{-0.03}$	$\lesssim 16.5$
PGMW 3223	21.4^d	267.8	$18.78^{+0.02}_{-0.01}$	$\lesssim 15.9$
'-'		287.8	$15.27^{+0.22}_{-0.17}$	$\lesssim 15.7$
Sk-66 35	20.83^d	264.4	$18.34^{+0.24}_{-0.18}$	$\lesssim 16.2$
'-'		275.4	$19.35^{+0.07}_{-0.02}$	$\lesssim 15.9$
'-'		286.0	$18.64^{+0.18}_{-0.13}$	$\lesssim 15.7$
Sk-69 52		248.8	$18.64^{+0.03}_{-0.02}$	$\lesssim 15.9$
Sk-65 21	< 20.50	247.8	$18.38^{+0.01}_{-0.01}$	$\lesssim 15.9$
Sk-66 51^e		311.5	$18.08^{+0.20}_{-0.20}$	$\lesssim 15.3$
Sk-70 79^f	21.26^d	234.6	$20.38^{+0.01}_{-0.01}$	$15.6^{+0.7}_{-0.5}$
Sk-68 52	21.30^d	248.8	$19.51^{+0.01}_{-0.01}$	$\lesssim 15.6$
Sk-71 8	21.04	186.6	$18.21^{+0.04}_{-0.07}$	$\lesssim 16.4$
'-'		220.4	$18.66^{+0.04}_{-0.03}$	$\lesssim 14.3$
Sk-70 85		256.7	$18.57^{+0.05}_{-0.04}$	$\lesssim 16.0$
		283.3	$17.18^{+0.18}_{-0.30}$	$\lesssim 15.9$
Sk-69 106		253.4	$18.78^{+0.02}_{-0.01}$	$\lesssim 15.6$
Sk-68 73^f	21.66^d	294.2	$20.24^{+0.01}_{-0.01}$	$14.2^{+0.1}_{-0.1}$
Sk-67 105	21.25^d	301.9	$19.42^{+0.05}_{-0.01}$	$\lesssim 14.8$
'-'		310.3	$17.46^{+0.29}_{-0.85}$	$\lesssim 13.9$
BI 184	21.12^d	240.4	$19.89^{+0.01}_{-0.02}$	$\lesssim 16.7$
'-'		281.2	$16.78^{+0.11}_{-0.20}$	$\lesssim 15.8$
Sk-71 38		201.3	$17.46^{+0.07}_{-0.07}$	$\lesssim 16.1$
		243.0	$18.53^{+0.06}_{-0.04}$	$\lesssim 16.0$
		280.1	$17.45^{+0.06}_{-0.05}$	$\lesssim 14.7$
Sk-71 45	21.09	254.1	$18.55^{+0.01}_{-0.01}$	$\lesssim 13.3$
Sk-71 46^f		243.4	$20.32^{+0.03}_{-0.01}$	$14.60^{+1.08}_{-0.30}$
Sk-69 191	20.78^d	229.2	$19.11^{+0.01}_{-0.02}$	$\lesssim 15.9$
'-'		257.7	$15.34^{+0.92}_{-0.30}$	$\lesssim 15.1$

Table 1 – *continued*

Star	$\log N\,(\mathrm{HI})^a$	ΔV^b, [km/s]	$\log N\,(\mathrm{H_2})$	$\log N\,(\mathrm{HD})^c$
J 0534-6932^f	21.60	270.6	$19.88^{+0.01}_{-0.01}$	$14.5^{+0.9}_{-0.4}$
'-'		294.3	$17.24^{+0.26}_{-0.41}$	$\lesssim 16.0$
BI 237^f	21.62	296.2	$20.20^{+0.01}_{-0.01}$	$14.4^{+1.0}_{-0.2}$
Sk-68 129	21.72	276.0	$20.53^{+0.07}_{-0.03}$	$\lesssim 17.2$
Sk-69 220	21.28	283.3	$19.29^{+0.01}_{-0.01}$	$\lesssim 16.4$
Sk-69 223	21.9	273.0	$19.18^{+0.08}_{-0.10}$	$\lesssim 16.3$
'-'		308.3	$19.94^{+0.01}_{-0.02}$	$\lesssim 16.2$
Sk-66 172	21.25	289.3	$18.18^{+0.08}_{-0.04}$	$\lesssim 16.1$
'-'		301.5	$16.62^{+0.49}_{-0.19}$	$\lesssim 16.1$
'-'		331.0	$16.35^{+0.30}_{-0.79}$	$\lesssim 14.9$
'-'		375.3	$15.97^{+0.38}_{-0.67}$	$\lesssim 15.5$
Sk-69 228	21.63	262.2	$18.28^{+0.03}_{-0.13}$	$\lesssim 16.8$
'-'		296.3	$18.87^{+0.06}_{-0.05}$	$\lesssim 16.4$
BI 253^f	21.67^d	267.3	$20.01^{+0.01}_{-0.01}$	$15.3^{+0.4}_{-0.9}$
'-'		279.9	$18.12^{+0.19}_{-0.35}$	$13.65^{+0.20}_{-0.23}$
Sk-68 135	21.46^d	250.7	$18.83^{+0.11}_{-0.06}$	$\lesssim 15.9$
'-'		272.4	$19.99^{+0.01}_{-0.01}$	$14.0^{+0.6}_{-0.3}$
Sk-68 137^f	21.50	278.5	$20.31^{+0.05}_{-0.32}$	$16.5^{+0.2}_{-1.6}$
'-'		302.9	$20.53^{+0.05}_{-0.11}$	$14.5^{+1.1}_{-0.3}$
Brey 77	21.79	277.1	$19.30^{+0.04}_{-0.06}$	$\lesssim 15.7$
'-'		296.1	$19.42^{+0.05}_{-0.04}$	$\lesssim 16.1$
'-'		316.4	$18.10^{+0.11}_{-0.11}$	$\lesssim 16.4$
Sk-69 243^e	21.80	271.0	$18.29^{+0.27}_{-0.19}$	$\lesssim 15.7$
'-'		280.3	$19.34^{+0.07}_{-0.05}$	$\lesssim 15.6$
'-'		290.0	$19.66^{+0.02}_{-0.04}$	$\lesssim 16.0$
'-'		312.4	$16.80^{+0.45}_{-0.16}$	$\lesssim 16.1$
Sk-69 246	21.47^d	273.0	$19.76^{+0.01}_{-0.01}$	$13.89^{+0.06}_{-0.06}$
Sk-68 140	21.47^d	275.6	$20.40^{+0.03}_{-0.03}$	$\lesssim 17.1$
Sk-71 50	21.18	238.2	$19.47^{+0.03}_{-0.04}$	$\lesssim 16.7$
'-'		267.5	$19.43^{+0.05}_{-0.05}$	$\lesssim 16.5$
'-'		292.1	$19.15^{+0.05}_{-0.07}$	$\lesssim 16.8$
Sk-69 279	21.59^d	249.4	$19.19^{+0.23}$	$\lesssim 17.1$
'-'		265.9	$20.54^{+0.01}_{-0.03}$	$\lesssim 17.0$
Sk-68 155	21.44^d	289.5	$20.02^{+0.03}_{-0.05}$	$\lesssim 16.8$
'-'		307.7	$19.03^{+0.40}_{-0.42}$	$\lesssim 16.4$
'-'		333.7	$19.00^{+0.22}_{-0.63}$	$\lesssim 17.0$
Sk-69 297		249.6	$19.77^{+0.03}_{-0.03}$	$\lesssim 16.3$
		295.1	$19.07^{+0.05}_{-0.05}$	$\lesssim 16.4$
Sk-70 115	21.13^d	215.6	$19.97^{+0.01}_{-0.01}$	$\lesssim 16.3$
'-'		292.1	$18.23^{+0.03}_{-0.02}$	$\lesssim 15.5$

a Total H I column density, taken from Welty et al. (2012), the typical uncertainty is about 10% (but the values were not shown by Welty et al. (2012)) except systems denoted by *d*
b Kinematic shift of the component relative to the local standard of rest.
c Upper limits were constrained from 3σ confidence interval.
d Taken from Roman-Duval et al. (2019).
e Low Doppler parameter, hence $\log N\,(\mathrm{H_2})$ may be overestimated.
f Systems with new HD detections.

Table 2. Fit results for HD and H_2 towards SMC.

Star	$\log N\,(\mathrm{HI})^a$	ΔV^b, [km/s]	$\log N\,(H_2)$	$\log N\,(\mathrm{HD})^c$
AV 6	21.54	107.4	$16.82^{+0.26}_{-0.46}$	$\lesssim 15.9$
'-'		132.0	$19.09^{+0.03}_{-0.02}$	$\lesssim 16.0$
'-'		150.5	$17.42^{+0.15}_{-0.67}$	$\lesssim 16.2$
AV 14	21.76	91.5	$15.69^{+0.44}_{-0.29}$	$\lesssim 14.4$
'-'		111.6	$18.18^{+0.07}_{-0.05}$	$\lesssim 14.1$
'-'		131.2	$18.33^{+0.07}_{-0.07}$	$\lesssim 15.3$
'-'		148.7	$16.60^{+0.25}_{-0.87}$	$\lesssim 15.4$
AV 15	21.58	119.9	$16.69^{+0.13}_{-0.12}$	$\lesssim 15.0$
		137.7	$18.45^{+0.01}_{-0.03}$	$\lesssim 15.3$
AV 16		128.0	$20.06^{+0.10}_{-0.07}$	$\lesssim 16.7$
		152.1	$19.99^{+0.10}_{-0.11}$	$\lesssim 16.4$
AV 18^f	22.04	103.4	$16.04^{+0.22}_{-0.15}$	$\lesssim 15.6$
'-'		130.6	$20.46^{+0.03}_{-0.02}$	$14.63^{+0.28}_{-0.20}$
'-'		154.2	$19.19^{+0.17}_{-0.26}$	$14.6^{+1.0}_{-0.2}$
'-'		176.0	$19.83^{+0.05}_{-0.06}$	$\lesssim 16.2$
AV 22	< 20.80	112.4	$18.06^{+0.06}_{-0.08}$	$\lesssim 16.0$
'-'		133.4	$17.50^{+0.18}_{-0.03}$	$\lesssim 15.8$
'-'		153.8	$17.48^{+0.14}_{-0.08}$	$\lesssim 16.2$
AV 26^f	21.70	119.3	$19.19^{+0.24}_{-0.22}$	$\lesssim 16.7$
'-'		132.5	$20.70^{+0.02}_{-0.01}$	$14.4^{+1.7}_{-0.4}$
'-'		152.0	$18.66^{+0.40}_{-0.77}$	$\lesssim 16.4$
AV 39a	21.74	103.7	$17.22^{+0.21}_{-0.26}$	$\lesssim 16.1$
'-'		117.1	$18.66^{+0.04}_{-0.04}$	$\lesssim 15.5$
'-'		129.8	$17.08^{+0.44}_{-0.22}$	$\lesssim 16.3$
AV 47	21.32	116.5	$17.72^{+0.07}_{-0.02}$	$\lesssim 15.4$
'-'		129.1	$18.45^{+0.02}_{-0.02}$	$\lesssim 13.5$
AV 60a	21.81	125.0	$18.76^{+0.13}_{-0.13}$	$\lesssim 15.9$
'-'		143.6	$19.72^{+0.02}_{-0.03}$	$\lesssim 16.6$
'-'		217.7	$18.12^{+0.15}_{-0.05}$	$\lesssim 16.1$
AV 69	21.59	112.8	$18.34^{+0.05}_{-0.05}$	$\lesssim 15.1$
'-'		128.4	$18.89^{+0.02}_{-0.02}$	$\lesssim 15.3$
AV 75	21.79	113.4	$18.87^{+0.01}_{-0.02}$	$\lesssim 15.3$
'-'		126.7	$17.74^{+0.11}_{-0.08}$	$\lesssim 13.7$
AV 80^f	21.81	118.8	$20.24^{+0.01}_{-0.01}$	$14.50^{+0.03}_{-0.04}$
'-'		135.0	$18.75^{+0.24}_{-0.86}$	$\lesssim 15.4$
AV 81		111.9	$15.99^{+0.18}_{-0.10}$	$\lesssim 15.1$
		139.8	$18.58^{+0.03}_{-0.02}$	$\lesssim 15.5$
		177.3	$17.88^{+0.04}_{-0.08}$	$\lesssim 13.8$
AV 95	21.49	93.7	$15.46^{+0.05}_{-0.06}$	$\lesssim 13.4$
'-'		124.5	$19.23^{+0.03}_{-0.04}$	$13.75^{+0.39}_{-0.29}$
'-'		139.0	$19.11^{+0.05}_{-0.05}$	$\lesssim 13.6$
AV 104	21.45	119.4	$19.35^{+0.01}_{-0.01}$	$\lesssim 16.1$
'-'		147.5	$16.77^{+0.28}_{-0.44}$	$\lesssim 15.9$

Table 2 – *continued*

Star	$\log N\,(\mathrm{HI})^a$	ΔV^b, [km/s]	$\log N\,(H_2)$	$\log N\,(\mathrm{HD})^c$
AV 170	21.14	138.1	$19.73^{+0.01}_{-0.01}$	$\lesssim 16.1$
AV 175		121.7	$19.49^{+0.17}_{-0.12}$	$\lesssim 16.6$
		138.5	$20.05^{+0.10}_{-0.09}$	$\lesssim 16.4$
NGC 346-12	21.81	138.9	$19.64^{+0.17}_{-0.07}$	$\lesssim 13.4$
'-'		166.5	$18.87^{+0.46}_{-0.51}$	$\lesssim 15.6$
'-'		183.3	$20.40^{+0.04}_{-0.06}$	$\lesssim 13.6$
AV 207	21.43	160.1	$19.52^{+0.02}_{-0.04}$	$\lesssim 16.8$
'-'		181.2	$18.93^{+0.08}_{-0.12}$	$\lesssim 16.5$
AV 208^f	21.85	160.1	$19.82^{+0.09}_{-0.12}$	$14.5^{+1.0}_{-0.3}$
'-'		181.2	$19.88^{+0.07}_{-0.16}$	$\lesssim 16.8$
AV 210	21.85	129.3	$19.33^{+0.01}_{-0.02}$	$\lesssim 16.1$
'-'		164.8	$17.62^{+0.26}_{-0.34}$	$\lesssim 16.6$
'-'		182.1	$17.34^{+0.16}_{-0.22}$	$\lesssim 16.5$
AV 215	21.86	126.2	$19.38^{+0.05}_{-0.10}$	$\lesssim 16.6$
'-'		145.7	$19.52^{+0.06}_{-0.05}$	$\lesssim 16.5$
AV 216	21.64	124.7	$17.68^{+0.16}_{-0.22}$	$\lesssim 15.7$
'-'		139.1	$18.71^{+0.05}_{-0.02}$	$\lesssim 16.0$
'-'		162.5	$15.99^{+0.31}_{-0.22}$	$\lesssim 16.2$
NGC 346-637	21.65	162.4	$19.44^{+0.02}_{-0.02}$	$\lesssim 17.0$
AV 243	21.52	128.4	$18.95^{+0.02}_{-0.02}$	$\lesssim 15.7$
'-'		147.9	$17.25^{+0.18}_{-0.30}$	$\lesssim 16.1$
AV 242^e	21.32	98.8	$17.18^{+0.14}_{-0.16}$	$\lesssim 14.0$
'-'		132.2	$15.00^{+0.16}_{-0.04}$	$\lesssim 15.7$
'-'		163.9	$17.73^{+0.08}_{-0.11}$	$\lesssim 15.9$
'-'		182.2	$16.75^{+0.14}_{-0.17}$	$\lesssim 14.9$
AV 261	21.43	93.2	$16.54^{+1.12}_{-0.37}$	$\lesssim 16.5$
'-'		125.3	$19.38^{+0.03}_{-0.03}$	$\lesssim 16.7$
AV 266		106.4	$17.01^{+0.27}_{-0.68}$	$\lesssim 15.2$
		127.3	$19.81^{+0.01}_{-0.02}$	$\lesssim 15.6$
		132.5	$17.46^{+0.44}_{-0.23}$	$\lesssim 15.5$
AV 304	21.48	121.0	$19.55^{+0.03}_{-0.03}$	$\lesssim 15.8$
'-'		137.6	$18.77^{+0.19}_{-0.27}$	$\lesssim 15.7$
AV 372^f	21.57	122.6	$15.52^{+0.15}_{-0.05}$	$\lesssim 15.6$
'-'		140.9	$18.62^{+0.04}_{-0.21}$	$\lesssim 16.2$
'-'		147.1	$18.45^{+0.10}_{-0.18}$	$13.97^{+0.22}_{-0.23}$
AV 374	21.14	86.5	$18.09^{+0.03}_{-0.04}$	$\lesssim 16.2$
'-'		133.1	$18.65^{+0.02}_{-0.02}$	$\lesssim 15.9$
AV 423	21.49	141.8	$18.00^{+0.36}_{-0.34}$	$\lesssim 15.5$
'-'		145.6	$18.49^{+0.10}_{-0.11}$	$\lesssim 14.2$
'-'		184.1	$17.03^{+0.28}_{-0.20}$	$\lesssim 16.1$
AV 435^f	21.54	177.4	$19.92^{+0.01}_{-0.01}$	$15.6^{+0.2}_{-0.8}$
AV 440	21.38	130.5	$17.29^{+0.04}_{-0.03}$	$\lesssim 14.8$
'-'		173.5	$19.06^{+0.01}_{-0.01}$	$\lesssim 15.8$
AV 472^f		137.8	$20.38^{+0.01}_{-0.01}$	$15.9^{+0.3}_{-0.8}$
AV 476	21.85	157.4	$20.84^{+0.03}_{-0.05}$	$\lesssim 17.1$
'-'		167.1	$19.79^{+0.21}_{-0.35}$	$\lesssim 17.1$

Table 2 – *continued*

Star	$\log N\,(\text{HI})^{a}$	ΔV^{b}, [km/s]	$\log N\,(\text{H}_2)$	$\log N\,(\text{HD})^{c}$
AV 479	21.42	152.1	$18.73^{+0.01}_{-0.02}$	$\lesssim 15.2$
	'-'	167.8	$18.99^{+0.01}_{-0.01}$	$\lesssim 15.4$
AV 480	21.42	183.8	$18.21^{+0.10}_{-0.16}$	$\lesssim 16.1$
	'-'	193.4	$18.53^{+0.07}_{-0.07}$	$\lesssim 16.2$
AV 483	21.13	145.9	$18.71^{+0.03}_{-0.04}$	$\lesssim 16.1$
	'-'	157.2	$18.48^{+0.06}_{-0.04}$	$\lesssim 16.4$
AV 486^{f}	21.18	145.5	$18.56^{+0.07}_{-0.07}$	$\lesssim 15.6$
	'-'	157.6	$19.07^{+0.02}_{-0.03}$	$14.0^{+0.9}_{-0.4}$
AV 488	21.15	146.6	$19.04^{+0.01}_{+0.03}$	$13.6^{+0.6}_{-0.5}$
	'-'	158.5	$18.96^{+0.03}_{-0.02}$	$\lesssim 14.6$
AV 490^{f}	21.46	132.0	$19.88^{+0.01}_{-0.01}$	$16.1^{+0.2}_{-0.7}$
	'-'	162.7	$17.94^{+0.29}_{-0.39}$	$\lesssim 15.6$
AV 491	21.40	97.7	$15.66^{+0.47}_{-0.71}$	$\lesssim 14.7$
	'-'	143.6	$18.99^{+0.05}_{-0.10}$	$\lesssim 15.5$
	'-'	155.6	$18.98^{+0.05}_{-0.26}$	$\lesssim 15.0$
	'-'	184.4	$15.09^{+0.81}_{-0.06}$	$\lesssim 14.6$
AV 506	21.35	132.3	$16.36^{+0.29}_{-0.12}$	$\lesssim 14.0$
	'-'	147.5	$19.03^{+0.01}_{-0.01}$	$\lesssim 15.7$
Sk 191^{f}	21.51	153.5	$20.78^{+0.02}_{-0.03}$	$14.7^{+1.2}_{-0.2}$
WR 9^{e}	21.48	87.7	$16.06^{+0.34}_{-0.25}$	$\lesssim 15.7$
	'-'	117.8	$18.69^{+0.08}_{-0.05}$	$\lesssim 15.9$
	'-'	135.5	$19.37^{+0.01}_{-0.02}$	$\lesssim 15.7$
	'-'	149.9	$16.43^{+0.42}_{-0.19}$	$\lesssim 15.7$
	'-'	167.9	$17.37^{+0.11}_{-0.44}$	$\lesssim 15.9$

a Total H I column density, taken from Welty et al. (2012)
b Kinematic shift of the component relative to the local standard of rest.
c Upper limits were constrained from 3σ confidence interval
e low Doppler parameter, $\log N\,(\text{H}_2)$ may be overestimated
f Systems with new HD detections.
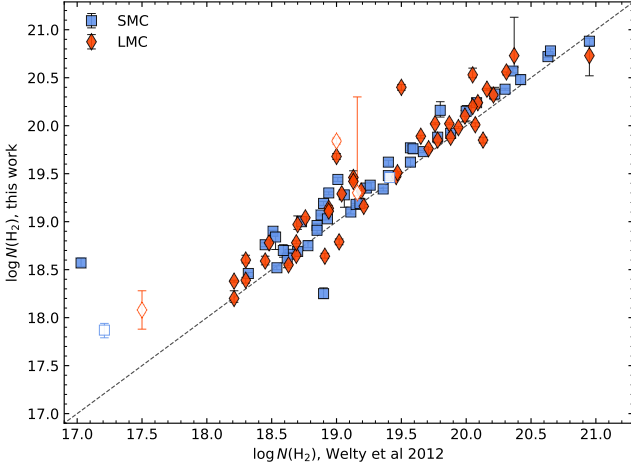
Figure 4. Comparison between the total H_2 column density estimates obtained by Welty et al. (2012) (x-axis) and our results (y-axis). The blue squares and red diamonds show measurements in SMC and LMC, respectively. Open symbols show systems with low Doppler parameters (for details see text). Dashed black line shows the one-to-one ratio.

5 COSMIC-RAY IONIZATION RATE

We used column densities, reported in the previous sections, to constrain physical conditions in the medium of LMC and SMC, associated with absorption systems. Among the parameters, listed above, in this work we focus mainly on CRIR (estimation of n, χ and metallicity in Magellanic Clouds will be presented in the accompanied paper, Kosenko et al in prep.) We followed the procedure developed and used for high-redshift systems in Kosenko et al. 2021.

This method is based on the balance equation between formation and destruction of HD molecules in the plane-parallel steady-state cloud, therefore leading to solve only one differential equation (Balashev & Kosenko 2020):

$$\frac{dN(HD)}{dN(H_2)} = f(\zeta, n, \chi, Z, N(H_2)),$$

except modelling of the cloud using full chemical network. Certainly to get reasonable constrain on CRIR this method requires an estimates of number density, UV field intensity and metallicity to remove degeneracy of parameters, which will be presented in Kosenko et al in prep. We fixed metallicity and used constraints on n and χ as priors during the Bayesian inference. For ζ we used flat priors in log space, emulating a wide distribution. We used Markov Chain Monte-Carlo method to estimate posterior distribution function on CRIR. Results are shown in the last column of Table 3.

Unfortunately, in the most sightlines except one, we get only upper limits on CRIR, ζ, due to large uncertainties in HD column density estimates (which is connected with insufficient quality of the data). In the systems, denoted by † in the Table 3, we could not constrain CRIR at all within the physically reasonable range $\lesssim 10^{-13}$, where the model from (Balashev & Kosenko 2020) is appropriate[4]. For these systems we got too wide posterior probabilities in this region (also due to the large uncertainties in $N(HD)$) encompassing all the range for ζ.

Constraints on CRIR as a function of H_2 column density are shown

Table 3. Physical conditions derived in the absorption systems associated with LMC and SMC.

Star	[X/H]	X	$\log n\,[\mathrm{cm}^{-3}]$	$\log \chi$	$\log \zeta\,[\mathrm{s}^{-1}]$
		LMC			
Sk-67 5†	$-0.58^{+0.05}_{-0.05}$	Zn	$1.99^{+0.17}_{-0.18}$	$0.40^{+0.19}_{-0.18}$	–
Sk-70 79†	$-0.63^{+0.06}_{-0.05}$	Zn	$2.75^{+0.36}_{-0.31}$	$1.81^{+0.21}_{-0.18}$	–
Sk-71 46	–	–	$2.50^{+0.32}_{-0.28}$	$1.24^{+0.27}_{-0.20}$	$\lesssim -15.8$
Sk-68 135†	$-0.67^{+0.06}_{-0.05}$	Zn	$2.00^{+0.20}_{-0.19}$	$1.62^{+0.31}_{-0.27}$	–
Sk-69 246	$-0.65^{+0.05}_{-0.05}$	Zn	$2.37^{+0.19}_{-0.17}$	$1.66^{+0.22}_{-0.22}$	$-16.73^{+0.29}_{-0.21}$
		SMC			
AV 26	$-0.96^{+0.06}_{-0.06}$	Zn	$2.02^{+0.22}_{-0.16}$	$0.35^{+0.61}_{-0.69}$	$\lesssim -17.0$
AV 80	$-1.16^{+0.05}_{-0.05}$	Zn	$3.89^{+0.15}_{-0.17}$	$2.01^{+0.31}_{-0.29}$	$\lesssim -16.5$
AV 372†	$-1.06^{+0.05}_{-0.05}$	Zn	$1.41^{+0.08}_{-0.10}$	$1.75^{+0.14}_{-0.10}$	–
AV 488	$-0.81^{+0.05}_{-0.06}$	Zn	$1.95^{+0.40}_{-0.35}$	$1.03^{+0.66}_{-0.55}$	$\lesssim -14.7$
AV 490†	$-1.06^{+0.05}_{-0.06}$	P	$2.01^{+0.11}_{-0.13}$	$1.38^{+0.18}_{-0.17}$	–
Sk 191	$-1.51^{+0.06}_{-0.06}$	Zn	$3.70^{+0.48}_{-0.68}$	$1.43^{+0.20}_{-0.26}$	$\lesssim -17.1$

The columns are: (i) name of the star; (ii) estimated metallicity; (iii) species that is used to derive metallicity; (iv) the number density; (v) the UV field strength in the units of Mathis field; (vi) the cosmic ray ionization rate.
Upper limits were constrained from 3σ credible interval
In the case of Sk-71 46 we have not found H I column density in the literature therefore we could not obtain metallicity for this system and to estimate CRIR we used an average metallicity of LMC ($Z = 0.5Z_\odot$)
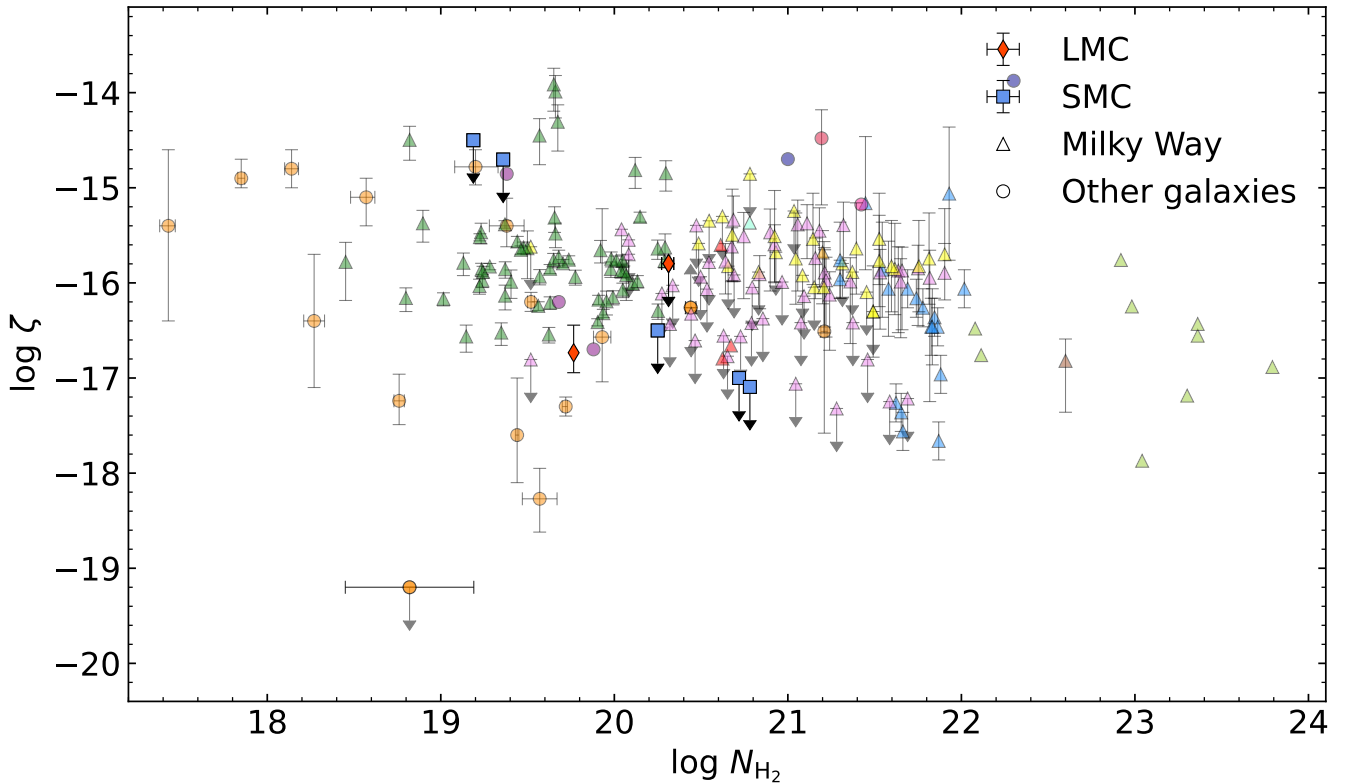† In these systems we could not constrain ζ (see the text)

in the Fig. 5 (red diamonds for the LMC and blue squares for the SMC) and compared to other known CRIR estimations in the Milky Way and other galaxies. Note that constraint on ζ in the system towards Sk 191 in the LMC should be taken with caution since we got metallicity about an order lower than average value in SMC and it may be attributed to the large depletion in this system (one of the highest value of H_2 column density also may point at this; details will be provided in Kosenko et al. in prep.).

6 DISCUSSION

Nevertheless that we detected HD towards two dozens of LMC and SMC sightlines, we could not obtain reasonable constraint on CRIR using HD/H_2. The reason is that we get insufficient constraints on the HD column density due to low quality of the FUSE spectra. To illustrate this in Fig. 6 we compare line profiles and estimates of the fitting parameters of HD obtained from the FUSE spectra towards AV 490 and mock high resolution spectrum (with $R = 50000$ and SNR=20). The original FUSE data indicates inability to remove degeneracy between high and low column density solutions, resulting in the wide (~ 2 dex) constraint on the column density. One can see that the usage of the higher resolution not only allow to decompose the two velocity components in HD lines, but significantly reduces the constrained interval for HD column density. Moreover, the inclusion of the weakest HD line L0-0R(0)[5] allows one to further shrink the

---

[4] For example, a very high CRIR may change chemistry of the cloud, due to destruction of molecules even in the self-shielded core, which is not considered in Balashev & Kosenko 2020

[5] note that L1-0(0) and L2-0R(0) are usually blended with H_2 absorption lines

Figure 5. The constraints on CRIR as a function of H$_2$ column density. Here blue squares and red diamonds are values obtained in this work (for SMC and LMC, respectively), circles are values found for other galaxies (orange - Kosenko et al. (2021), blue - Muller et al. (2016), violet - Shaw et al. (2016), pink - Indriolo et al. (2018)), triangles are values for our Galaxy (yellow - Indriolo et al. (2007), light green - table 6 from Padovani et al. (2009), blue - Caselli et al. (1998), cyan - Shaw et al. (2008), brown - Maret & Bergin (2007), violet - Indriolo & McCall (2012), dark green - Indriolo et al. (2015))

interval and to get the uncertainties comparable to what is obtained for HD in high redshift DLAs (see e.g. Kosenko et al. 2021). This situation is similar to the case of the galactic sightlines, where HD measurement are also shallow, while typically galactic sightlines have higher SNR, which can reduce the uncertainty, but cannot remove the degeneracy. The lower uncertainty of HD column density will allow to get more strict constraints on CRIR, instead of upper limits obtained using FUSE real data, as is shown in the right panel of Fig. 6. Therefore, the next generation of the space UV telescopes, equipped with high resolution spectrograph will allow to constrain the CRIR using HD/H$_2$ ratio, that will provide important insights on the cold diffuse medium of the Magellanic clouds, as well as in our Galaxy.

7 SUMMARY

We have provided a systematic search for HD molecules in the LMC and SMC, the closest low-metallicity dwarf galaxies, using FUSE archival data. To make analysis homogeneous we reanalyzed H$_2$ using multicomponent Voight profile fitting of H$_2$ J $\lesssim$ 5 rotational levels. On the positions of H$_2$ components we looked for HD molecules. Although the quality of the FUSE data allows to obtain in the most cases only upper limits on HD column densities, we detected HD towards 24 sightlines (including 19 new detection).

In six systems (out of 24 where we have detected HD) we obtained constraints on CRIR, and in five among them we could place only upper limits, mostly due to large uncertainties in HD column density

estimation. In the five systems we could not obtain reasonable constraints on the CRIR due to the too wide form of posterior probability functions, which cover all of the range within reasonable range of CRIR.

We also discuss influence of the spectral resolution on the results of our analysis and show that increase of the resolution of data will result in decrease of the column density uncertainties, which allows to obtain strict constraints on CRIR.

DATA AVAILABILITY

The results of this paper are based on open data retrieved from the FUSE telescope archive. These data can be shared on reasonable requests to the authors.

REFERENCES

Ackermann M., et al., 2016, Astron. Astroph., 586, A71
André M. K., et al., 2004, Astron. Astroph., 422, 483
Balashev S. A., Kosenko D. N., 2020, MNRAS, 492, L45
Balashev S. A., Varshalovich D. A., Ivanchik A. V., 2009, Astronomy Letters, 35, 150
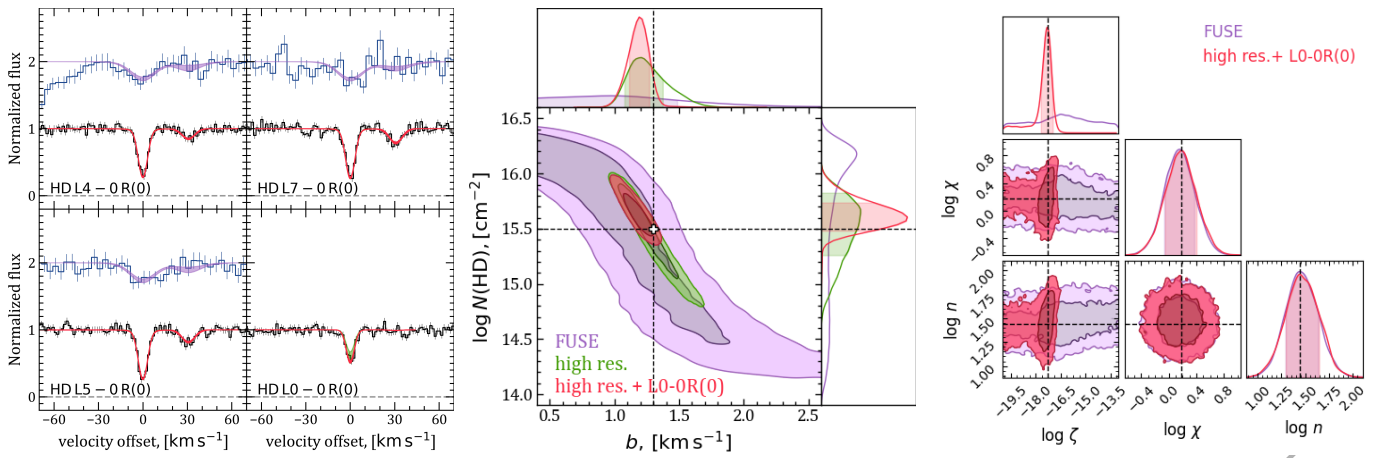
Figure 6. *Left*: The profiles of selected HD lines. The blue and black lines show the real FUSE spectrum of AV 490 (shifted by 1 vertically for the presentation purposes) and the mock high resolution spectrum. To generate the mock spectrum we assume, that the $b = 1.3 \, \text{km s}^{-1}$ and $\log N \, (\text{HD}) = 15.5$ (shown by cross at the middle panel). The fits to HD line profiles using two component Voigt function are shown by lavender, green and red lines and correspond to FUSE (using L4-0R(0), L5-0R(0), L7-0R(0)), mock (the same sample of HD lines) and mock with additionally taking into account L0-0R(0) line, respectively. *Middle*: The 2d posterior in the Doppler parameter - column density space, obtained during the fit to HD lines. The color correspond to the fit shown in left panel. *Right*: The constraints on the CRIR using estimates of HD column density from FUSE spectrum (lavender lines and regions) and from high-resolution mock spectrum (red).

Balashev S. A., Petitjean P., Ivanchik A. V., Ledoux C., Srianand R., Noterdaeme P., Varshalovich D. A., 2011, MNRAS, 418, 357

Black J. H., Dalgarno A., 1973, Astroph. J. Lett., 184, L101

Blair W. P., Oliveira C., LaMassa S., Gutman S., Danforth C. W., Fullerton A. W., Sankrit R., Gruendl R., 2009, Pub. Astron. Soc. Pacific, 121, 634

Bluhm H., de Boer K. S., 2001, Astron. Astroph., 379, 82

Carswell R. F., Jorgenson R. A., Wolfe A. M., Murphy M. T., 2011, MNRAS, 411, 2319

Caselli P., Walmsley C. M., Terzieva R., Herbst E., 1998, Astroph. J., 499, 234

Dixon W. V., et al., 2007, Pub. Astron. Soc. Pacific, 119, 527

Dufton P. L., Ryans R. S. I., Thompson H. M. A., Street R. A., 2008, MNRAS, 385, 2261

Graczyk D., et al., 2020, Astroph. J., 904, 13

Gvaramadze V. V., Pflamm-Altenburg J., Kroupa P., 2011, Astron. Astroph., 525, A17

Hartquist T. W., Black J. H., Dalgarno A., 1978, MNRAS, 185, 643

Hindman J. V., Kerr F. J., McGee R. X., 1963, Australian Journal of Physics, 16, 570

Indriolo N., McCall B. J., 2012, Astroph. J., 745, 91

Indriolo N., Geballe T. R., Oka T., McCall B. J., 2007, Astroph. J., 671, 1736

Indriolo N., et al., 2015, Astroph. J., 800, 40

Indriolo N., Bergin E. A., Falgarone E., Godard B., Zwaan M. A., Neufeld D. A., Wolfire M. G., 2018, Astroph. J., 865, 127

Ivanchik A. V., Balashev S. A., Varshalovich D. A., Klimenko V. V., 2015, Astronomy Reports, 59, 100

Kosenko D. N., Balashev S. A., Noterdaeme P., Krogager J. K., Srianand R., Ledoux C., 2021, MNRAS, 505, 3810

Lee J. K., Rolleston W. R. J., Dufton P. L., Ryans R. S. I., 2005, Astron. Astroph., 429, 1025

Lehner N., Howk J. C., Keenan F. P., Smoker J. V., 2008, Astroph. J., 678, 219

Lopez L. A., Auchettl K., Linden T., Bolatto A. D., Thompson T. A., Ramirez-Ruiz E., 2018, Astroph. J., 867, 44

Maret S., Bergin E. A., 2007, Astroph. J., 664, 956

Moos H. W., et al., 2000, Astroph. J. Lett., 538, L1

Muller S., et al,, 2016, Astron. Astroph., 595, A128

Niemela V. S., Morrell N. I., 1986, Astroph. J., 310, 715

Noterdaeme P., Ledoux C., Petitjean P., Le Petit F., Srianand R., Smette A., 2007, Astron. Astroph., 474, 393

Noterdaeme P., et al., 2017, Astron. Astroph., 597, A82

Noterdaeme P., Balashev S., Krogager J. K., Srianand R., Fathivavsari H., Petitjean P., Ledoux C., 2019, Astron. Astroph., 627, A32

Ostrov P. G., Lapasset E., 2003, MNRAS, 338, 141

Padovani M., Galli D., Glassgold A. E., 2009, Astron. Astroph., 501, 619

Pietrzyński G., et al., 2019, Nature, 567, 200

Planck Collaboration et al., 2020, Astron. Astroph., 641, A6

Ramachandran V., Oskinova L. M., Hamann W. R., 2021, Astron. Astroph., 646, A16

Roman-Duval J., et al., 2019, Astroph. J., 871, 151

Russell S. C., Dopita M. A., 1992, Astroph. J., 384, 508

Sahnow D. J., et al., 2000, Astroph. J. Lett., 538, L7

Savage B. D., Sembach K. R., 1991, Astroph. J., 379, 245

Shaw G., Ferland G. J., Srianand R., Abel N. P., van Hoof P. A. M., Stancil P. C., 2008, Astroph. J., 675, 405

Shaw G., Rawlins K., Srianand R., 2016, MNRAS, 459, 3234

Shull J. M., 2022, Physics Today, 75, 12

Shull J. M., Danforth C. W., Anderson K. L., 2021, Astroph. J., 911, 55

Simkin S. M., 1974, Astron. Astroph., 31, 129

Snow T. P., Ross T. L., Destree J. D., Drosback M. M., Jensen A. G., Rachford B. L., Sonnentrucker P., Ferlet R., 2008, Astroph. J., 688, 1124

Tonry J., Davis M., 1979, Astron. J., 84, 1511

Tumlinson J., et al., 2010, Astroph. J., 718, L156

Ubachs W., Salumbides E. J., Murphy M. T., Abgrall H., Roueff E., 2019, Astron. Astroph., 622, A127

Varshalovich D. A., Ivanchik A. V., Petitjean P., Srianand R., Ledoux C., 2001, Astronomy Letters, 27, 683

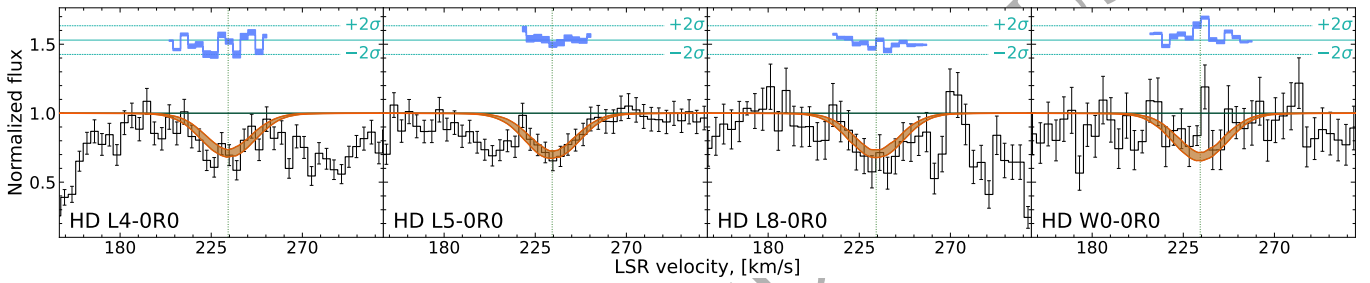Welty D. E., Xue R., Wong T., 2012, Astroph. J., 745, 173
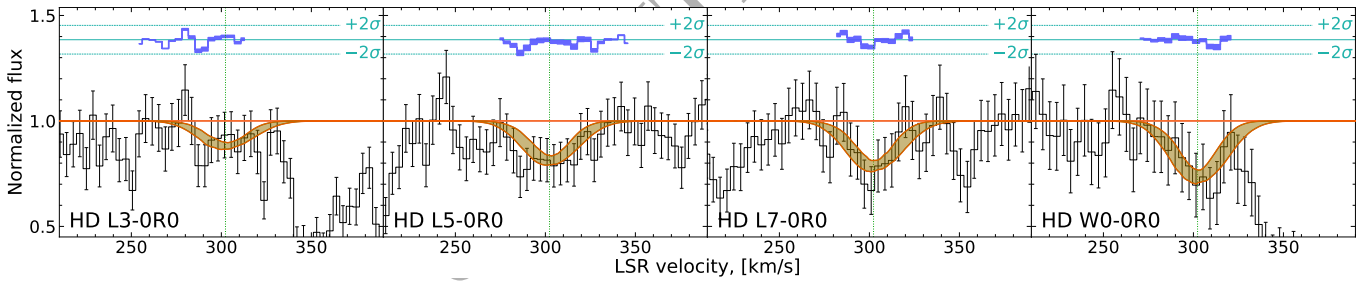
APPENDIX A: NEW HD DETECTIONS
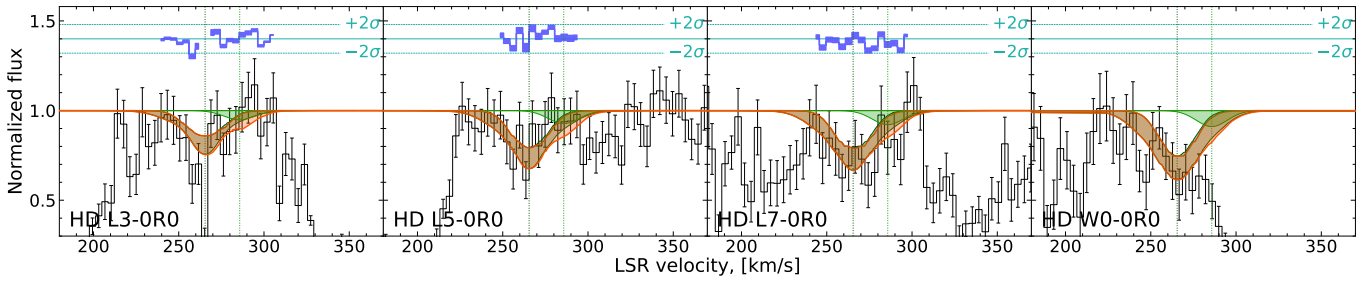
Figure A1. Fit to HD absorption lines towards LH10 3073 in LMC. Lines are the same as for 1.
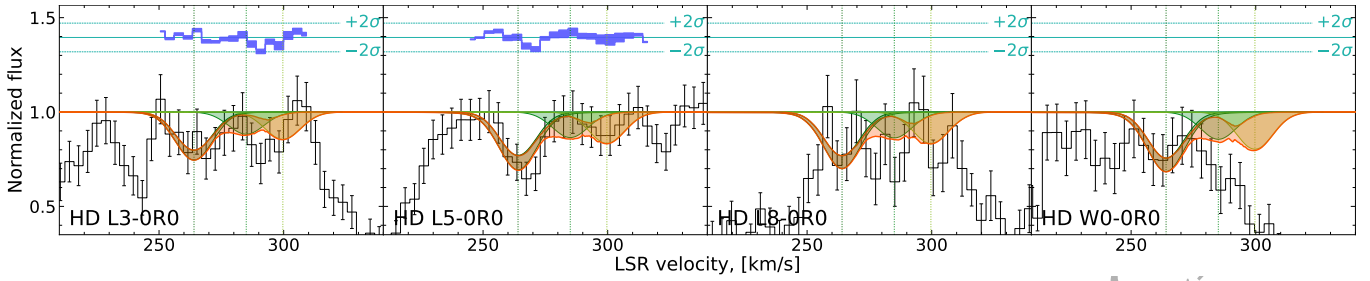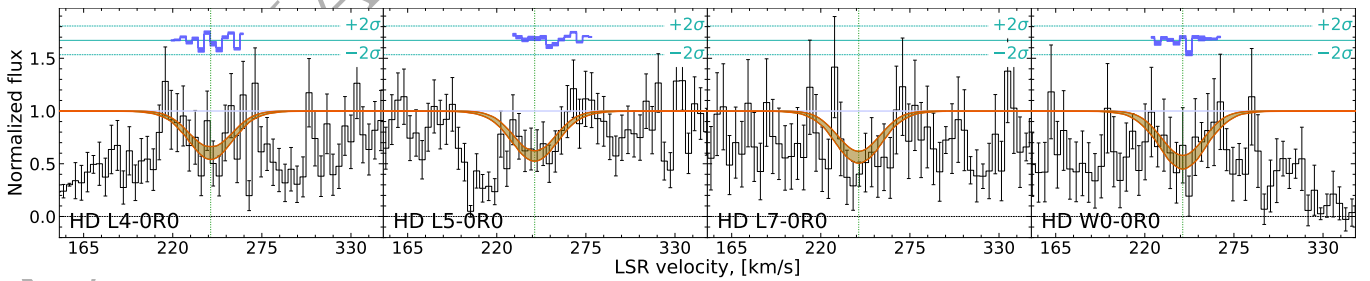
Figure A2. Fit to HD absorption lines towards LH10 3102 in LMC. Lines are the same as for 1.

Figure A3. Fit to HD absorption lines towards Sk-70 79 in LMC. Lines are the same as for 1.

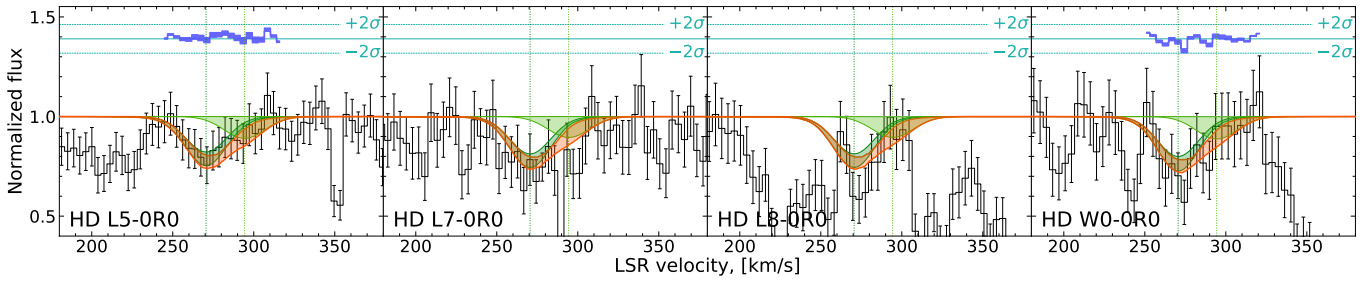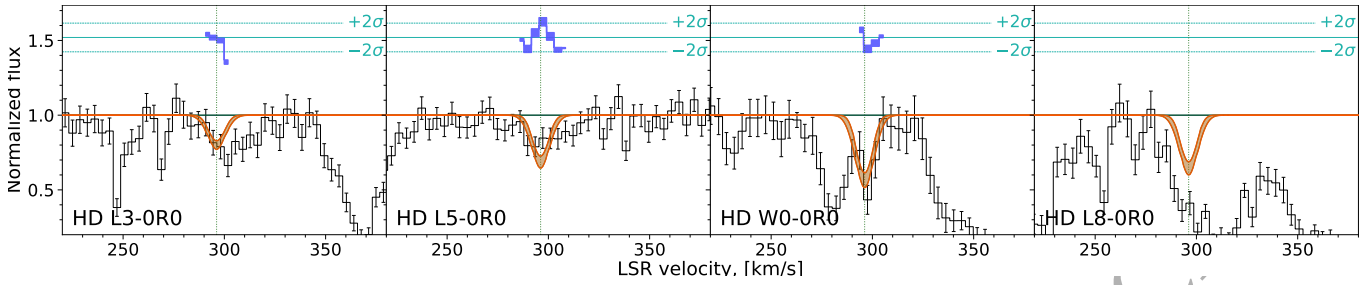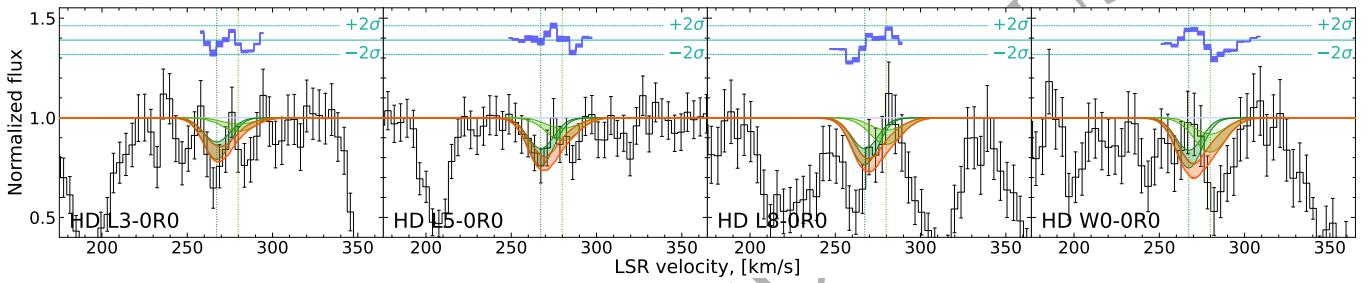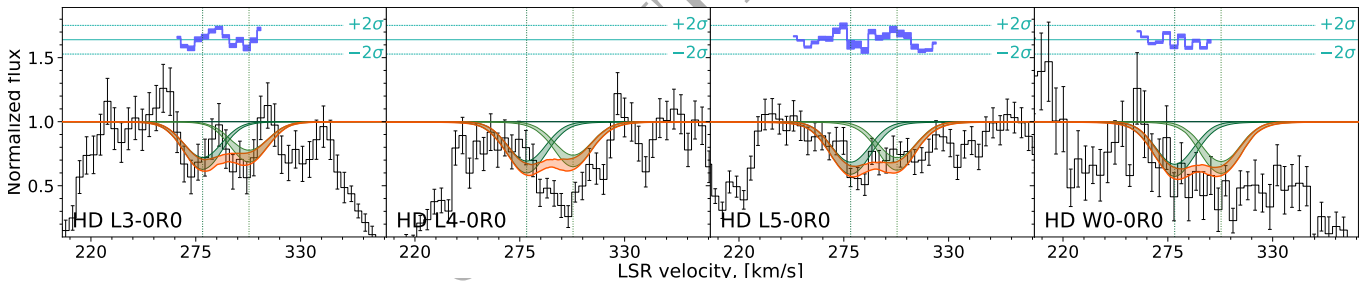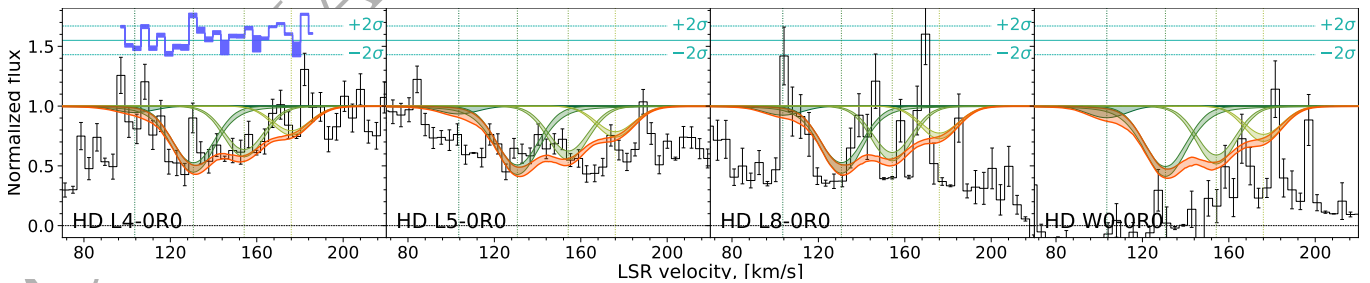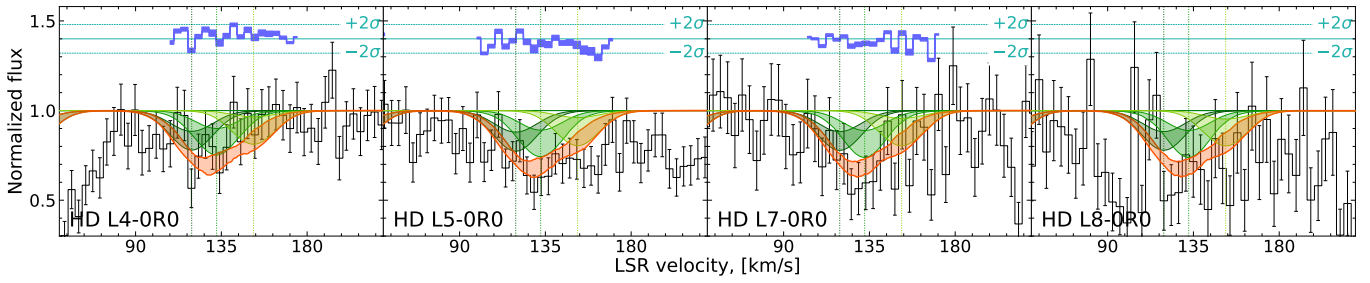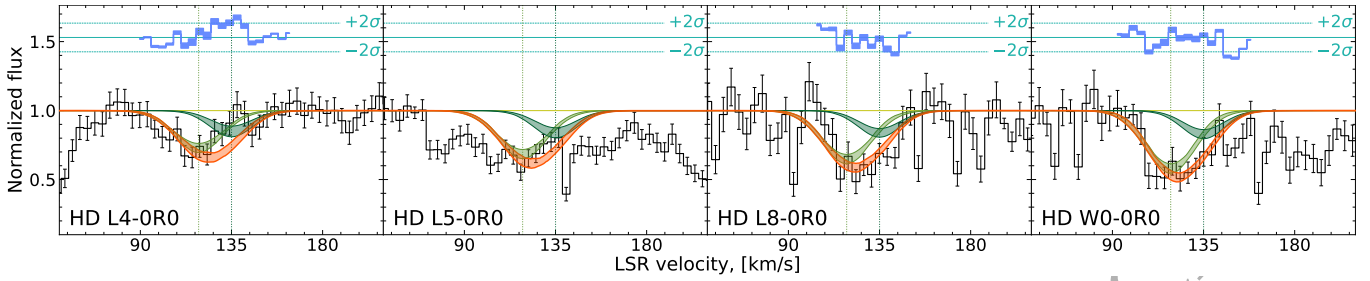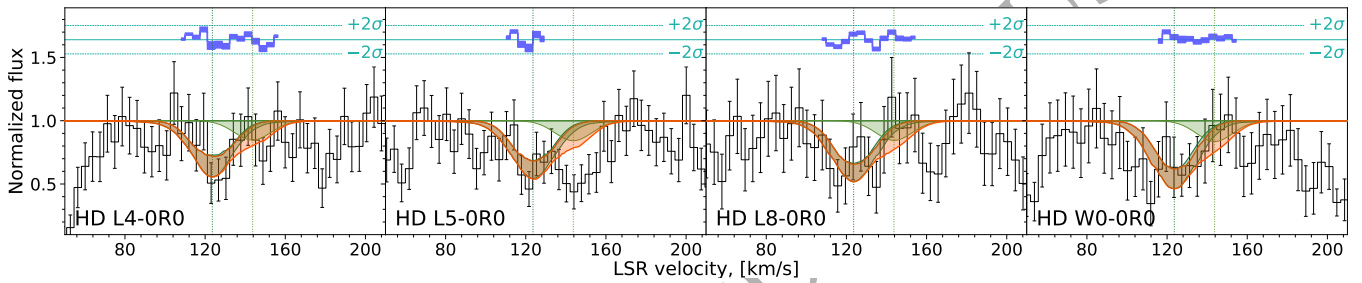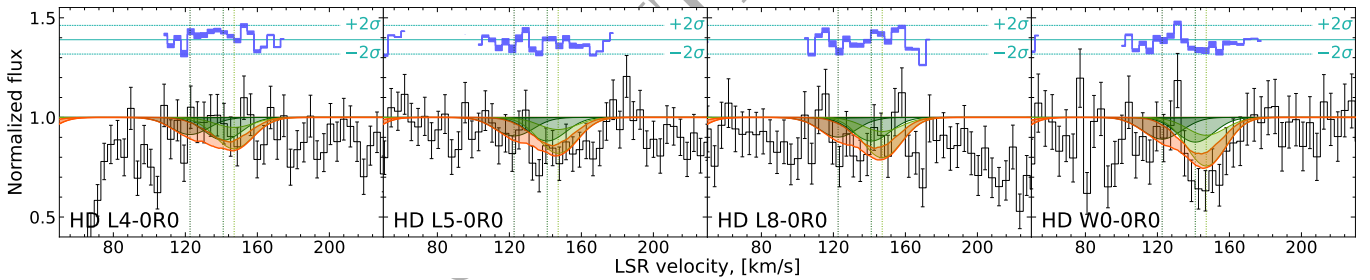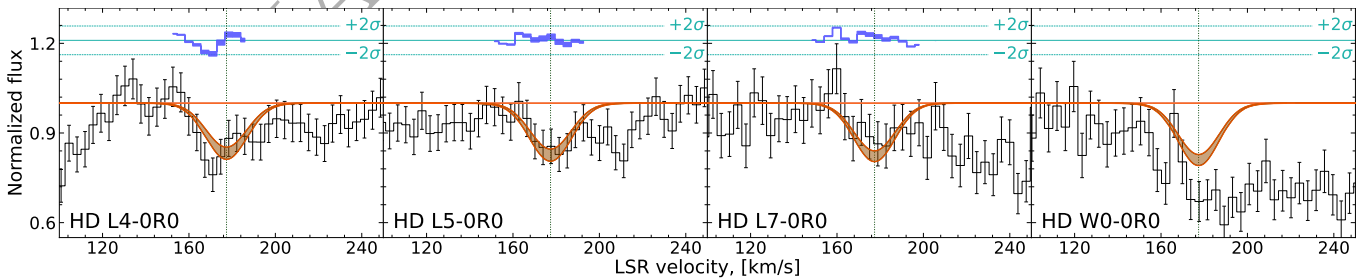**Figure A4.** Fit to HD absorption lines towards Sk-68 73 in LMC. Lines are the same as for 1.

Figure A5. Fit to HD absorption lines towards Sk-71 46 in LMC. Lines are the same as for 1.

Figure A6. Fit to HD absorption lines towards J 0534-6932 in LMC. Lines are the same as for 1.

Figure A7. Fit to HD absorption lines towards BI 237 in LMC. Lines are the same as for 1.

Figure A8. Fit to HD absorption lines towards BI 253 in LMC. Lines are the same as for 1.

Figure A9. Fit to HD absorption lines towards Sk-68 137 in LMC. Lines are the same as for 1.

Figure A10. Fit to HD absorption lines towards AV 18 in SMC. Lines are the same as for 1.

Figure A11. Fit to HD absorption lines towards AV 26 in SMC. Lines are the same as for 1.

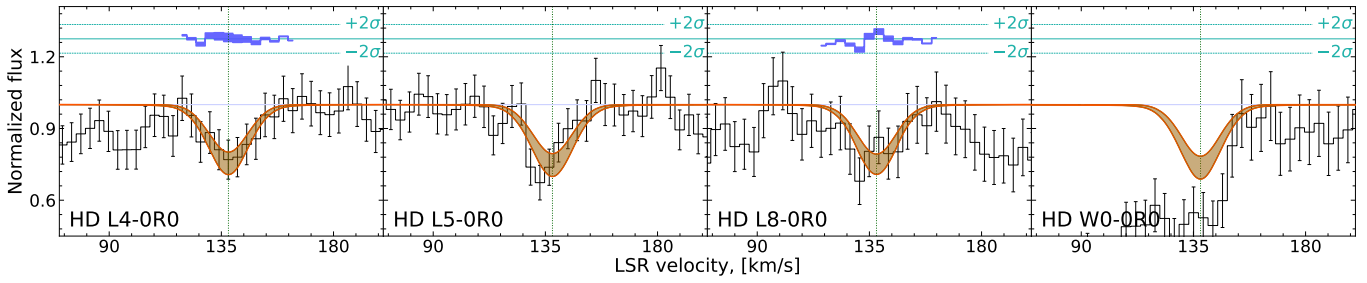**Figure A12.** Fit to HD absorption lines towards AV 80 in SMC. Lines are the same as for 1.

Figure A13. Fit to HD absorption lines towards AV 208 in SMC. Lines are the same as for 1.

Figure A14. Fit to HD absorption lines towards AV 372 in SMC. Lines are the same as for 1.

Figure A15. Fit to HD absorption lines towards AV 435 in SMC. Lines are the same as for 1.

Figure A16. Fit to HD absorption lines towards AV 472 in SMC. Lines are the same as for 1.
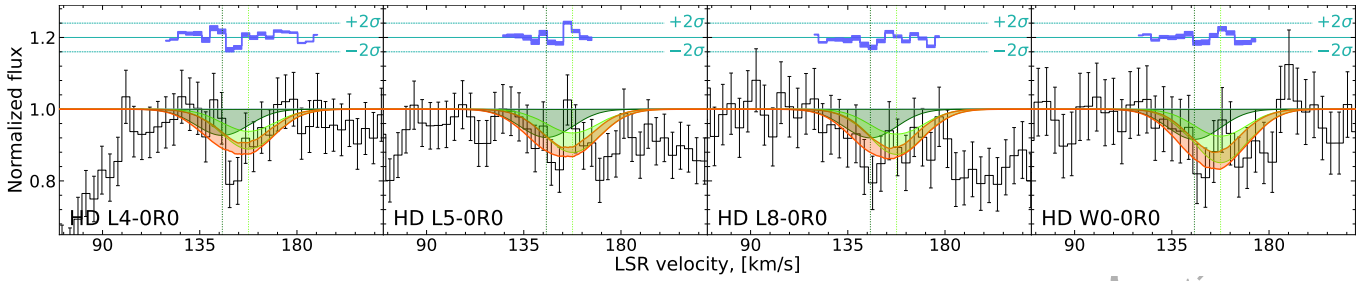
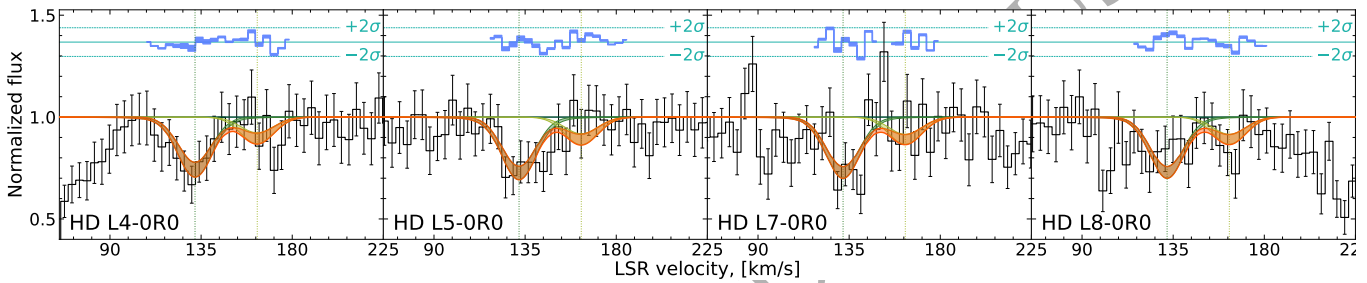**Figure A17.** Fit to HD absorption lines towards AV 486 in SMC. Lines are the same as for 1.

Figure A18. Fit to HD absorption lines towards AV 490 in SMC. Lines are the same as for 1.